Ultrasonics 168 (2026) 108241

Contents lists available at ScienceDirect

Ultrasonics

journal homepage: www.elsevier.com/locate/ultras

LSMS-Net: Resolving multiple scattering via physics-constrained deep learning for photoacoustic imaging in porous media

Wenyi Xu [a,d], Renzhe Bi [d], Weiya Xie [f], Lifang Jin [b], Malini Olivo [d], Shengsong Huang [e,*], Ya Gao [a,b,c,**], Qian Cheng [a,b,c,**]

[a] Institute of Acoustics, School of Physics Science and Engineering, Tongji University, Shanghai 200092, China
[b] Department of Ultrasonography, Shanghai Disabled Persons' Federation Key Laboratory of Intelligent Rehabilitation Assistive Devices and Technologies, Yangzhi Rehabilitation Hospital (Shanghai Sunshine Rehabilitation Center), Tongji University School of Medicine, Shanghai 201619, China
[c] National Key Laboratory of Autonomous Intelligent Unmanned Systems, Shanghai Research Institute for Intelligent Autonomous Systems, Tongji University, Shanghai 201210, China
[d] A*STAR Skin Research Laboratories (A*SRL), Singapore 138669, Singapore
[e] Department of Urology, Tongji Hospital, Tongji University School of Medicine, Shanghai 200065, China
[f] College of Underwater Acoustic Engineering, Harbin Engineering University, Harbin 150001, China

ARTICLE INFO

Keywords:
Photoacoustic Imaging
Porous Heterogeneous Media
Layer-Stripping
Physics-Constrained Deep Learning
Frequency-Dependent Attenuation

ABSTRACT

Photoacoustic imaging of porous heterogeneous media is fundamentally challenged by spatially distributed optical absorbers that simultaneously serve as acoustic scatterers. This dual role causes multiple scattering, wavefront distortion, and frequency-dependent attenuation, which cannot be decoupled by conventional homogeneous-medium reconstruction algorithms. As a result, deep-tissue images suffer from severe image blurring and irreversible loss of high-spatial-frequency microstructural details. To address this, we propose a physics-constrained deep learning framework termed the Layer-Stripping Multi-Scattering Network (LSMS-Net), which recursively solves the inverse multiple scattering problem. LSMS-Net implements a top-down, curriculum-driven strategy to progressively estimate propagation-induced effects and correct raw measurements layer by layer. The framework integrates a Ghost Network for non-local reverberation, an Adaptive Scattering Point Spread Function Layer for wavefront distortion, and a Spectral Consistency Constraint for frequency-dependent attenuation. Quantitative evaluation via numerical simulations and phantom experiments confirms accurate, high-fidelity reconstruction of deep porous structures under strongly scattering, showing potential for clinical application in bone-related diseases.

1. Introduction

Photoacoustic imaging (PAI) integrates the high optical absorption contrast with the high resolution and deep penetration capability of ultrasound, thereby enabling quantitative, multiscale assessment of both structural and functional properties in biological complex media [1,2]. Although PAI has demonstrated robust performance in homogeneous soft tissues [3,4], its extension to acoustically two-phase porous heterogeneous media, such as cancellous bone [5,6], lung tissue [7], or engineered composite foams [8,9], remains technically challenging. In such media, acoustic wave propagation is influenced by spatial variations in acoustic impedance, density, and compressibility. As a result, conventional assumptions, such as homogeneity or weak-scattering approximations, fail to accurately capture the underlying physics.

In acoustically heterogeneous and two-phase porous media, the primary challenge in PAI arises from path-accumulated multiple scattering rather than isolated, target-invariant single-scattering events. When optical absorption is distributed volumetrically, acoustic waves generated at different depths undergo different propagation paths before reaching the transducer. First, spatial acoustic impedance mismatches at solid–liquid interfaces induce strong scattering, manifesting as reflections and reverberations [10,11]. As illustrated in Fig. 1(b-1), repeated partial reflections between adjacent structures generate coherent reverberation clutter that degrades time-resolved PA signals. Second, as shown in Fig. 1(b-2), such scattering leads to cumulative wavefront distortion during propagation. In porous media such as

* Corresponding author.
** Corresponding authors at: Institute of Acoustics, School of Physics Science and Engineering, Tongji University, Shanghai 200092, China.
E-mail addresses: hssfline@tongji.edu.cn (S. Huang), y.gao@tongji.edu.cn (Y. Gao), q.cheng@tongji.edu.cn (Q. Cheng).

https://doi.org/10.1016/j.ultras.2026.108241
Received 28 April 2026; Received in revised form 29 June 2026; Accepted 20 July 2026
Available online 22 July 2026
0041-624X/© 2026 The Authors. Published by Elsevier B.V. This is an open access article under the CC BY-NC license (http://creativecommons.org/licenses/by-nc/4.0/).

cancellous bone, trabecular simultaneously serve as optical absorbers and acoustic scatterers. Because the characteristic dimensions of trabecular are comparable to the acoustic wavelength, wave propagation undergoes complex scattering including Mie scattering (ka ≈ 1) [12,13], leading to pronounced angular redistribution and phase distortion. The accumulation of these effects results in a depth-dependent and spatially variant system response that cannot be described by a shift-invariant point spread function (PSF) [14,15]. Third, frequency-dependent attenuation in porous media arises from the combined effects of multiple scattering and viscous losses. According to Biot's theory, porous two-phase media exhibit enhanced attenuation of high-frequency acoustic components due to pore-scale viscous dissipation and scattering at heterogeneous interfaces [16], as illustrated in Fig. 1(b-3). Consequently, PA signals generated at greater depths undergo progressive bandwidth reduction, leading to loss of fine structural detail and blurred distal features. Collectively, the combined effects of reverberation, wavefront distortion, and frequency-dependent attenuation induce severe, depth-dependent, and spatially variant image degradation in PAI, highlighting the need for imaging algorithms that account for multiple scattering and shift-variant acoustic impulses responses.

Existing PA reconstruction methods face fundamental limitations in strongly scattering and acoustically heterogeneous media. Conventional reconstruction algorithms, such as delay-and-sum (DAS) and filtered back-projection (FBP), rely on the assumption of a spatially uniform sound speed, leading to significant degradation in spatial resolution and quantitative accuracy in heterogeneous tissues [17,18]. Ray-based compensation methods improve upon DAS by incorporating refraction effects along geometric ray paths. However, their underlying ray approximation ignores diffraction and multiple scattering, rendering them inadequate for media with strong, dense scattering [19]. In contrast, wave-physics-driven approaches, including time-reversal (TR) [20] and full-wave iterative reconstruction [21,22], theoretically accommodate acoustic heterogeneity by solving the exact PA (or coupled thermoelastic) wave equation. Yet their practical efficacy depends on accurate prior knowledge of the medium's sound speed and density distributions. Crucially, in PAI, the scatterers responsible for heterogeneity constitute the unknown targets of interest, resulting in such high-fidelity priors are inherently inaccessible. Iterative implementations of these methods require computational costs due to repeated forward and adjoint wave simulations. Alternatively, linear model-based methods formulate the forward problem as a discrete matrix equation ($\mathbf{p} = \mathbf{A}\mathbf{x}$) [23,24]. Recent advancements have adopted frequency-domain formulations to accelerate this process, achieving near real-time performance by pre-calculating the system matrix [25]. Nevertheless, this efficiency gain does not solve the limitation that constructing an accurate system matrix still requires the same precise background acoustic property map just as full-wave methods.

More recently, deep learning (DL) has emerged as a powerful paradigm for image reconstruction and artifact suppression. Pure data-driven networks, such as U-Net and its variants [26–28], typically operate as black-box models that neglect the underlying wave propagation physics, resulting in limited generalizability across diverse acoustic environments. To bridge this gap, model-based learning (MBL) frameworks, represented by deep gradient descent [29], have been proposed. By casting iterative optimization algorithms as trainable neural networks layers, these approaches enforce strong data consistency while preserving interpretability. However, MBL frameworks rely on simplified fixed forward operators derived under homogeneous or weak-scattering assumptions, which limits their ability to model the complex multiple scattering, wavefront distortion, and non-local reverberation in porous two-phase media. Therefore, there remains an urgent need for a physics-constrained deep learning framework that decouples the source and scatterer contributions to achieve accurate structural imaging in such acoustically complex media.

To overcome these limitations, we propose the Layer-Stripping Multi-Scattering Network (LSMS-Net), a physics-constrained framework designed to PAI reconstruction in two-phase porous media. We employ a layer-stripping strategy for inverse scattering problems with depth-dependent multiple scattering in stratified media and adopts an analysis-by-synthesis strategy iteratively updates the solution. Accurate estimation of the near-field optical absorption allows the scattering contribution to deeper regions to be predicted through forward simulation and removed during the reconstruction. LSMS-Net uses a recursive optimization loop in which a differentiable forward physical simulator predicts the cumulative scattering field from the current

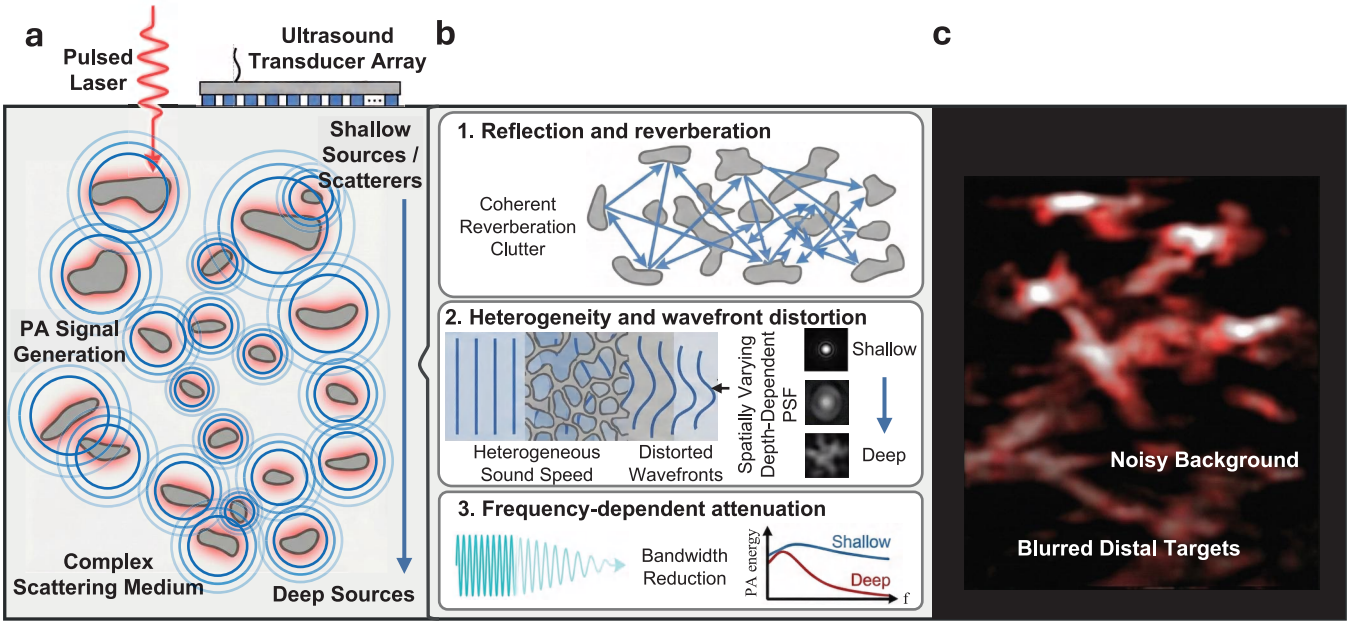


Fig. 1. Photoacoustic degradation in two-phase porous scattering media. (a) Imaging geometry in which targets act simultaneously as PA sources and acoustic scatterers. Shallow structures introduce strong scattering that disrupts wave propagation from deeper sources. (b) Three physical factors influencing reconstruction quality. (c) Delay-and-sum reconstruction showing background noise and blurred deep targets.

source estimation at each iteration. This simulator comprises two physics-aware components. First, an Adaptive Scattering Point Spread Function Layer models statistical wavefront distortion by integrating a physical derived Gaussian main lobe with learnable side lobes to capture heterogeneous scattering signatures. Second, the Ghost Network employs multi-scale dilated convolutions with progressively expanding receptive fields to represent non-local reverberation effects. Furthermore, to address the resolution loss caused by frequency-dependent attenuation in porous media, we introduce a spectral consistency constraint. Based on the differential attenuation characteristics of porous media, this constraint encourages consistency between the predicted and reference spectra in the logarithmic frequency domain, helping deep features retain edge sharpness and textural fidelity.

We validate LSMS-Net through a comprehensive dual-validation strategy involving both k-Wave simulations and experiments on 3D-printed phantoms. The phantoms are designed with controllable porous structures to mimic the acoustic complexity of natural porous media. The simulations assess the network's ability to disentangle overlapping scattering effects, while the phantom experiments demonstrate its robustness and practical applicability under realistic experimental conditions. Our results demonstrate that by progressively removing scattering layers and enforcing spectral validity, LSMS-Net significantly outperforms existing baselines in terms of signal-to-noise ratio (PSNR), structural similarity index (SSIM), and multi-scale SSIM (MS-SSIM), and robustly recovers obscured deep microstructures with enhanced spatial resolution and morphological fidelity.

2. Method

2.1. Physics problem formulation

We consider the PAI problem in a heterogeneous porous medium Ω. Denote $y(\mathbf{r})$ as the spatially varying optical absorption distribution (the source to be reconstructed) at location $\mathbf{r} \in \Omega$. Under the standard thermoelastic approximation and assuming negligible thermal diffusion, the measured acoustic pressure $x(\mathbf{r}_d, t)$ at detector position $\mathbf{r}_d$ is governed by the PA wave equation [30]. Consequently, x can be expressed as the output of a non-linear forward operator $\mathscr{A}$ acting on y and the spatially dependent acoustic parameters as Eq.(1) [21]:

$$x = \mathscr{A}(y, \boldsymbol{c}(y), \boldsymbol{\rho}(y)) + \eta \tag{1}$$

where η denotes additive measurement noise (e.g., electronic or thermal noise), and $\boldsymbol{c}(\bullet)$ and $\boldsymbol{\rho}(\bullet)$ denote the spatial distributions of sound speed and mass density, both of which are coupled to y through the microstructure (eg., solid–fluid phase fractions). In porous bone-like media, the structures that generate the initial PA pressure also affect acoustic propagation by creating local impedance contrasts, which lead to scattering, refraction, and attenuation.

Physically, $\mathscr{A}$ represents the solution operator to the PA wave equation, which can be expressed via Green's function integral as Eq.(2):

$$x(\mathbf{r}_d, t) = \int_{\Omega} G(\mathbf{r}_d, t; \mathbf{r}, 0) * \frac{\partial}{\partial t} y(\mathbf{r}) \mathrm{d}\mathbf{r} + \eta \tag{2}$$

where, $G(\mathbf{r}_d, t; \mathbf{r}, 0)$ represents the time-dependent Green's function describing the impulse response from source location $\mathbf{r}$ to detector $\mathbf{r}_d$, including all orders of reflection, scattering, and attenuation [31]. Unlike in homogeneous media, where $G(\bullet)$ reduces to a simple retarded spherical wave, $G(\bullet)$ in porous media is intrinsically non-local, depth-dependent, and highly sensitive to microstructural geometry.

This structural coupling distinguishes PAI in porous media from conventional PAI in a fixed acoustic background. In this setting, absorbers are not only passive PA sources; they also act as acoustic scatterers, and their spatial arrangement directly affects wave propagation. To describe this process, we decompose the forward model into two components: (i) A structure-dependent reverberation term $\mathscr{G}(y)$, representing non-local multipath interference arising from closed-loop wave propagation; and (ii) an adaptive transmission term $\mathscr{H}(y) \otimes y$, where $\mathscr{H}(y)$ is a spatially variant convolutional kernel describing cumulative forward multiple scattering, including wavefront distortion, dispersion, and path-length–dependent attenuation. The resulting forward model is therefore:

$$x \approx \mathscr{G}(y) + \mathscr{H}(y) \otimes y \tag{3}$$

Here, $\otimes$ denotes a spatially varying filtering operation, and both $\mathscr{G}(y)$ and $\mathscr{H}(y)$ are functions of y determined by the local density and arrangement of scattering structures, reflecting the inseparability of source and scatterer. Thus, the reconstruction task is to invert this nonlinear, y-coupled system to recover y from x.

LSMS-Net learns an approximate inverse mapping $\mathscr{T}_{\Theta} : \mathscr{X} \to \mathscr{Y}$ from the scattered observation domain $\mathscr{X}$ to the source domain $\mathscr{Y}$, where Θ denotes the full set of trainable parameters of LSMS-Net. The optimal parameters $\widehat{\Theta}$ are obtained by solving the following regularized reconstruction problem:

$$\widehat{\Theta} = \underset{\Theta}{\operatorname{argmin}} \sum\nolimits_i \left(\| \mathscr{T}_{\Theta}(x_i) - y_i \|_2^2 + \lambda \mathscr{R}(\mathscr{T}_{\Theta}(x_i), y_i) \right) \tag{4}$$

where (x_i, y_i) represents the paired scattered observation and ground-truth source distribution, $\mathscr{R}(\bullet)$ denotes a physics-informed regularization term, implemented here as spectral consistency, and λ balances the regularization term against the spatial reconstruction fidelity term. The explicit form of this regularization and the final unrolled training objective are introduced in the following sections.

2.2. Layer-Stripping Multi-Scattering network (LSMS-Net)

Directly solving Eq. (4) is ill-posed because the inverse problem involves strong nonlinearity, high dimensionality, and scattering physics coupled to the unknown source distribution y. To address this, we propose the LSMS-Net, which unrolls the inverse problem into a recursive sequence of T layer-stripping iterations using an analysis-by-synthesis strategy. The overall network architecture is illustrated in Fig. 2.

Denote $y^{(k-1)}$ as the estimated source distribution from the previous iteration (initialized as $y^{(0)} = \mathbf{0}$). The update rule at each iteration, as shown in Fig. 2a, is formulated as:

$$x_{sim}^{(k)} = \Phi_{fwd}\left(y^{(k-1)}\right) \tag{5}$$

$$\Delta y^{(k)} = \Psi_{solver}\left(x, x_{sim}^{(k)}, y^{(k-1)}, \mathscr{S}^{(k)}\right) \tag{6}$$

$$y^{(k)} = \mathscr{P}_{+}\left(y^{(k-1)} + \Delta y^{(k)}\right) \tag{7}$$

Here, $\Phi_{fwd}(\bullet)$ is a differentiable, physics-constrained forward simulator that approximates the scattering-aware forward model in Eq. (3). $\mathscr{S}^{(k)}$ denotes the scattering potential map estimated from the current input estimate $y^{(k-1)}$, with $\mathscr{S}^{(k)}(z)$ representing its depth-dependent value. This map serves as an auxiliary input to the solver and provides spatial information about accumulated scattering strength. $\Psi_{solver}(\bullet)$ predicts a residual correction that aligns the simulated data with the measurement, and $\mathscr{P}_{+}(\bullet)$ is the non-negative projection operator ensuring physical validity.

Specifically, the physics-constrained forward simulator $\Phi_{fwd}(\bullet)$, denoted as the 'Physical synthesis module' in Fig. 2a, models the structure-dependent scattering field within each iteration. It comprises two differentiable modules that implement the adaptive transmission operator $\mathscr{H}\left(y^{(k-1)}\right) \otimes y^{(k-1)}$ and reverberation operators $\mathscr{G}\left(y^{(k-1)}\right)$ with their parameters learned under explicit physical constraints:

Ghost Network ($\mathscr{G}$): To model non-local reverberation arising from backscattering and closed-loop multipath propagation, such as round-trip reflections between adjacent pore walls, we introduce a dedicated

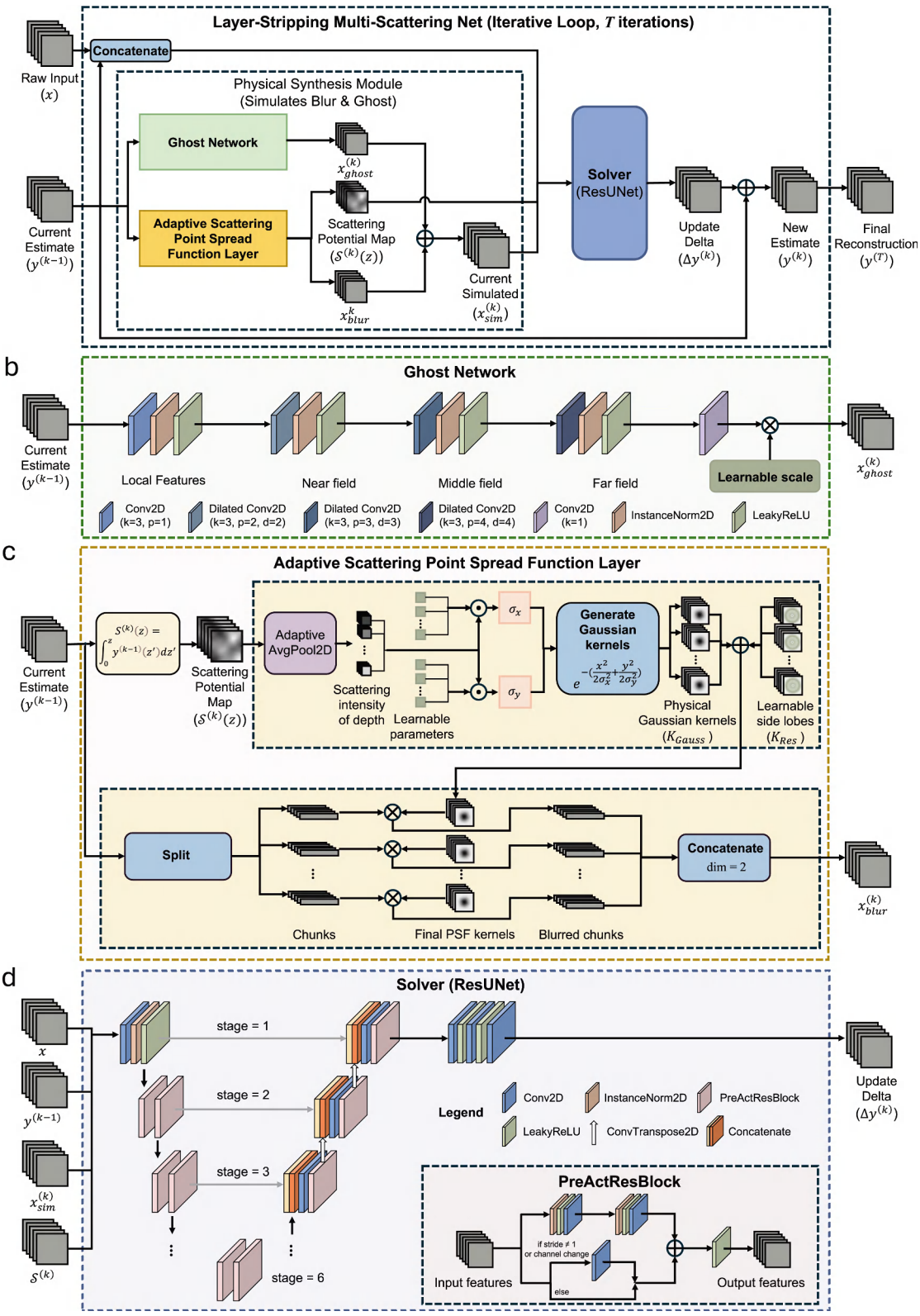


Fig. 2. Architecture of the proposed LSMS-Net. (a) Overview of the main network pipeline. The forward process unfolds over T iterations. In each iteration, the Adaptive Scattering Point Spread Function Layer and the Ghost Network serve as physical operators to generate simulated measurements based on the current object estimate. The Solver then computes the update for the next step using the raw input, the current estimate, the simulated image, and the scattering map. (b) The learnable Ghost Network, designed to simulate reverberation artifacts. (c) Structure of the Adaptive Scattering Point Spread Function Layer, which models the scattering PSF by integrating a physics-based Gaussian kernel with learnable side-lobe components. (d) The Solver module, implemented using a ResUNet architecture.

subnetwork composed of stacked dilated convolutions (Fig. 2b). Dilated convolutions exponentially expand the receptive field without loss of spatial resolution, allowing the network to model long-range multipath interference [32]. Specifically, as illustrated in Fig. 2b, the Ghost Network consists of stacked dilated convolution blocks with dilation rates of 2, 3, and 4, which are used to capture near-, middle-, and far-field reverberation patterns, respectively. A learnable scaling factor then adjusts the strength of the predicted ghost artifact before it is added to the synthesized signal. Ghost Network takes the current source estimate $y^{(k-1)}$ as input and predicts the ghost artifacts ($x_{ghost}^{(k)} \approx \mathscr{G}(y^{(k-1)})$) generated by distal scattering, where $\mathscr{G}(\bullet)$ denotes the complex reverberation operator defined in Eq. (3).

Adaptive Scattering Point Spread Function Layer ($\mathscr{K}$): As shown in Fig. 2c, this layer models wavefront distortion caused by forward multiple scattering in heterogeneous porous media. To balance physical fidelity and representational flexibility, we decompose the adaptive PSF into a physics-based main-lobe component and a learnable residual side-lobe component:

$$PSF^{(k)}(z) = K_{Gauss}\left(\sigma^{(k)}(z)\right) + K_{Res}(\theta_{res}) \tag{8}$$

i. Scattering Main Lobe (K_{Gauss}): A depth-adapted Gaussian kernel models the dominant forward-scattering main lobe. This Gaussian approximation is motivated by the central-limit behavior of accumulated phase perturbations under weak-to-moderate forward multiple scattering [33,34] (see Supplementary Materials for details). The kernel width $\sigma^{(k)}(z)$ varies with depth and represents progressive coherence loss along the propagation path. In practice, the accumulated scattering strength is approximated by a depth-integrated surrogate map $\mathscr{S}^{(k)}(z) = \int_0^z y^{(k-1)}(z')dz'$. As z increases, $\sigma^{(k)}(z)$ becomes wider, reflecting stronger wavefront broadening through multiple scattering layers.

ii. Complex Side Lobes (K_{Res}): A learnable residual kernel $K_{Res}(\theta_{res})$, with θ_{res} representing the module-specific trainable parameters within the overall parameter set Θ, is added to capture non-Gaussian and asymmetric side lobes that are not described by the Gaussian approximation. These components include higher-order diffraction patterns, directional bias, and interference fringes arising from strong local impedance contrasts and deviations from paraxial or second-order statistical assumptions. Unlike hand-crafted side-lobe models, K_{Res} can adapt to medium-specific scattering characteristics through learning.

The blurred image component is thus $x_{blur}^{(k)} = y^{(k-1)} \bigotimes PSF^{(k)}$.

The total simulated observation is given by $x_{sim}^{(k)} = x_{blur}^{(k)} + x_{ghost}^{(k)}$.

Instance-Aware Solver (Ψ_{solver}): Ψ_{solver} estimates the source update $\Delta y^{(k)}$ from raw input x, the current absorption estimate $y^{(k-1)}$, the corresponding physics-based forward prediction $x_{sim}^{(k)}$, and the scattering potential map $\mathscr{S}^{(k)}(z)$. This design allows the update $\Delta y^{(k)}$ to depend on the local scattering distribution, rather than treating $x - x_{sim}^{(k)}$ as a spatially uniform residual.

We implement Ψ_{solver} (Fig. 2d) as a compact ResUNet variant with skip-connected encoder-decoder blocks. To preserve sample-wise physical fidelity in heterogeneous porous media where scattering statistics vary substantially between samples, we replace batch normalization with instance normalization (IN).

2.3. Spectral consistency loss with Curriculum-Guided optimization

A fundamental consequence of acoustic wave propagation in porous media is frequency-dependent attenuation, which causes spectral redshift and loss of high-frequency microstructural details. Standard mean square error (MSE) loss often fails to recover these details because it treats all spatial frequencies equally and does not account for the physics-driven decay profile. To address this, the physics-informed regularization term $\mathscr{R}(\bullet)$ in Eq. (4) is implemented as a spectral consistency constraint. The loss is defined in the logarithmic power spectrum domain:

$$\mathscr{L}_{spec}^{(k)} = \left\|\log\left(\left|\mathrm{FFT}\left(y^{(k)}\right)\right| + \epsilon\right) - \log\left(\left|\mathrm{FFT}\left(y_{gt}\right)\right| + \epsilon\right)\right\|_1 \tag{9}$$

where FFT denotes the 2D Fourier transform, ϵ is a stability term, and y_{gt} denotes the ground-truth source distribution. This loss can be interpreted as a spectral-domain constraint that encourages compensation for frequency-dependent attenuation.

To further address the depth-dependent signal degradation in porous media, we incorporate a physically grounded spatial weighting mechanism. Acoustic waves originating from deeper regions traverse longer scattering paths, leading to increased energy attenuation and more severe signal-to-noise ratio (SNR) degradation compared to shallow regions. In this setting, standard MSE loss is dominated by high-amplitude shallower signals, leading to under-penalization of deeper regions. To compensate for this, we define the depth weight as:

$$W_{depth}(z,k) = 1 + \alpha \bullet k \bullet z \tag{10}$$

where $\alpha > 0$ is a tunable scaling factor and $z \in [0,1]$ denotes the normalized depth (z = 0 at the surface and z = 1 at the maximum imaging depth). At early iterations (small k), $W_{depth} \approx 1$, the weight is approximately uniform, allowing the network to learn global features. As k increases, the weight shifts toward deeper regions, increasing the contribution of depth-suppressed targets.

The total objective function integrates the depth-weighted reconstruction loss and the spectral consistency regularization within a staged optimization framework:

$$\mathscr{L}_{total} = \sum_{k=1}^{T} \omega_k \left(\left\| \left(y^{(k)} - y_{gt}\right) \odot \sqrt{W_{depth}(z,k)} \right\|_2^2 + \lambda \mathscr{L}_{spec}^{(k)} \right) \tag{11}$$

where ω_k increases with iteration k, assigning greater weight to later refinement stages, and λ balances spectral fidelity against spatial reconstruction accuracy. Thus, Eq. (11) represents the unrolled training objective corresponding to the regularized formulation in Eq. (4).

3. Simulation and experiment

3.1. Network Implementation and training

A unified computational pipeline was adopted for all simulation and experimental studies presented in this work. For both datasets described in the following sections, PA images were reconstructed using the DAS algorithm and paired with their corresponding μ-CT reference images. The resulting paired datasets were randomly partitioned into training, validation, and testing sets in a 7:2:1 ratio, respectively.

The unrolling depth T of the proposed LSMS-Net was set to 4, based on empirical evaluation through ablation studies. Network training was conducted using a two-stage strategy. Specifically, the model was first trained on the simulation dataset and subsequently fine-tuned on the experimental phantom dataset using the pre-trained weights. This training protocol enabled consistent initialization and parameter transfer across simulation and experimental domains.

All training and inference procedures were implemented in Python 3.11 using PyTorch 2.0.1. All computations were conducted on a computer with an AMD EPYC 9534 64-Core Processor @ 2.45 GHz, an NVIDIA RTX 6000 Ada Generation GPU, and 512 GB of RAM.

3.2. Simulation

k-Wave Simulation Setup: We employed high-resolution μ-CT images from six porcine cancellous bone specimens as anatomically

realistic physical models of porous scattering media. To obtain a sufficient number of samples for deep learning training, multiple circular ROIs were extracted from each specimen. All selected ROIs were spatially non-overlapping to reduce direct structural duplication. Each ROI was 256 pixels in diameter, corresponding to 6.8 mm, and was binarized to generate 7272 ground-truth absorption maps representing heterogeneous trabecular architectures. The resulting ROI samples were randomly divided into training, validation, and testing sets with a ratio of 7:2:1.

Acoustic simulations were performed using the k-Wave Toolbox in Matlab [35], with a temporal sampling interval of 1 ns over a total acquisition window of 15 μs. The initial PA pressure was defined from the binarized μ-CT-derived trabecular maps, where the solid trabecular regions were assigned an initial pressure of 1 and the soft-tissue-like background was assigned 0. This setting models the target porous bone-like scenario in which trabecular structures serve as the dominant optical absorbers and generate PA signals under around 690 nm excitation corresponding to the characteristic absorption of hydroxyapatite-related bone matrix components [6,36,37], while the same structures also introduce acoustic scattering. The resulting acoustic wave propagation was simulated and detected by a 128-element linear-array transducer. Spatially varying acoustic properties were incorporated, with sound speed set to 3200 m/s in mineralized trabecular bone and 1500 m/s in soft-tissue-like regions, and mass density set to 2000 kg/m^3 and 1000 kg/m^3, respectively [31,38,39]. The simulated RF signals were reconstructed into initial PA images using DAS beamforming algorithm, and the corresponding μ-CT-derived binary absorption maps served as quantitative ground truth for training and evaluation. The simulation pipeline is illustrated in Fig. 3a.

Results: Fig. 4 presents representative k-Wave simulation results across a range of porosity levels (75%, 70%, 65%, and 60%) [40,41]. Here, porosity was calculated as the area fraction of the black void region within the circular sample region inscribed in each square image. The first row shows the μ-CT-derived binary absorption images serving as ground truth. The second row shows the DAS reconstructions serving as network inputs, which exhibit progressive degradation with increasing depth, including structural blurring, loss of trabecular continuity, and attenuation of fine morphological details. The third row shows the reconstructions obtained by the proposed LSMS-Net, which consistently recovers clear structural features across all porosity levels, providing reliable recovery even for deep targets that are poorly resolved in DAS. In contrast to DAS, the proposed method significantly suppresses scattering-induced artifacts and restores high-fidelity microstructures, demonstrating robust reconstruction performance under highly heterogeneous scattering conditions.

Fig. 5 illustrates the iterative reconstruction behavior of LSMS-Net for a representative k-Wave simulation sample. As shown in Fig. 5(e), the reconstructed structures progressively extend from the shallow layers toward deeper regions from iteration 1 to iteration 4. The corresponding update maps are displayed in Fig. 5(b), where regions with higher update intensity are initially concentrated near the surface and gradually appear at greater depths in subsequent iterations. Fig. 5(d) shows the depth-wise intensity distributions of the update maps at each iteration. A distinct downward shift in the peak update energy is observed, demonstrating the depth-dependent nature of the process. Finally, the final estimated scattering map (Fig. 5(c)) spatially aligns with structural features in the ground truth shown in Fig. 5(a).

3.3. Experiment

3D-Printed Phantom Experiments: To validate real-world applicability, we fabricated anatomically accurate 3D-printed polylactic acid (PLA, density ≈ 1.25 g/cm^3, longitudinal sound speed ≈ 2246 m/s [42,43]) scaffolds directly segmented and scaled from μ-CT-derived micro-architectural patterns. Interstitial voids were filled with commercially available unsalted butter (fat content > 96%, density ≈

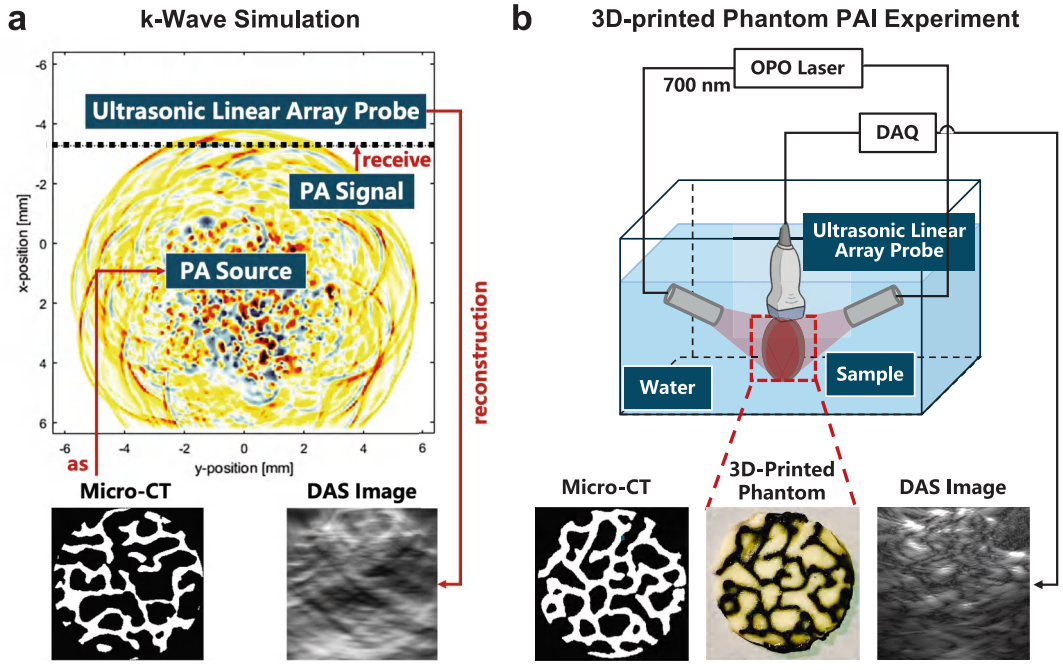


Fig. 3. Numerical simulation and physical phantom experimental setups. (a) Schematic of the k-Wave simulation study. The μ-CT image serves as the structural reference, where the white regions represent the trabecular bone matrix and the black regions represent the soft-tissue-like pore space. The simulation models both the spatially distributed PA source derived from optical absorption and the subsequent acoustic wave propagation. (b) Experimental setup for the 3D-printed phantom study. The phantom is immersed in a water tank for acoustic coupling. Its skeleton is fabricated via fused deposition modeling (FDM) using black polylactic acid (PLA), representing the trabecular bone structure, with geometry directly segmented and scaled from the μ-CT image. The internal voids are filled with butter (yellow regions) to approximate the acoustic impedance and attenuation characteristics of soft tissue. The bottom row shows (left to right) the μ-CT-derived structural map, a photograph of the assembled phantom, and the corresponding DAS reconstruction image.

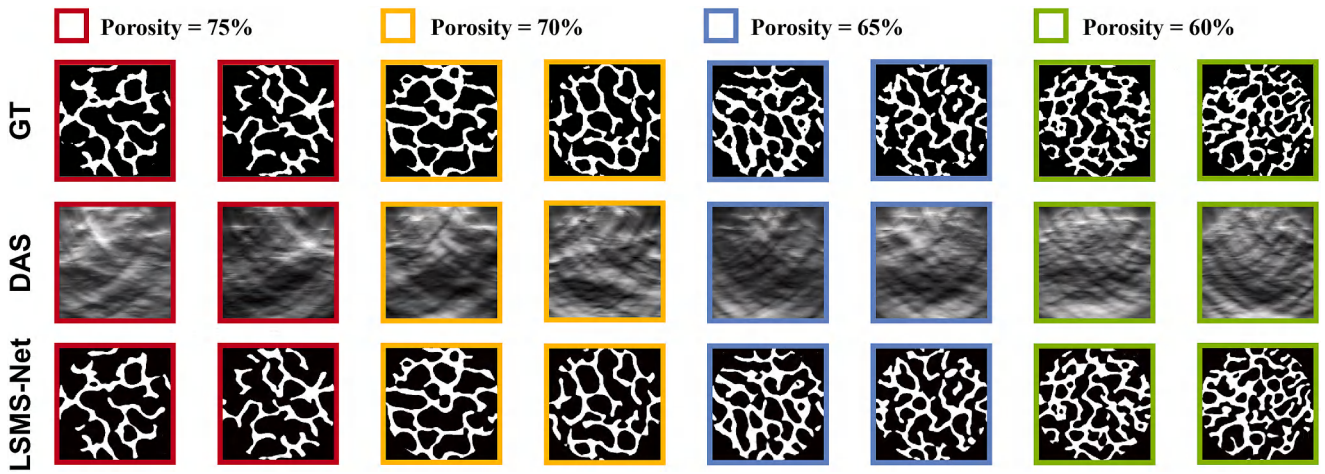


Fig. 4. K-wave simulation results under different porosity conditions (75%, 70%, 65%, and 60%). Porosity was defined as the area fraction of the black void region within the circular sample region inscribed in each square image; therefore, lower porosity corresponds to a larger solid trabecular fraction and a denser microstructure. From top to bottom: μ-CT-derived absorption images serving as ground-truth, DAS reconstruction (network input), and LSMS-Net reconstruction (network output). DAS reconstructions exhibit severe image degradation and loss of deep structural details under strong scattering, whereas LSMS-Net consistently restores clear and continuous structures across different porosity levels.

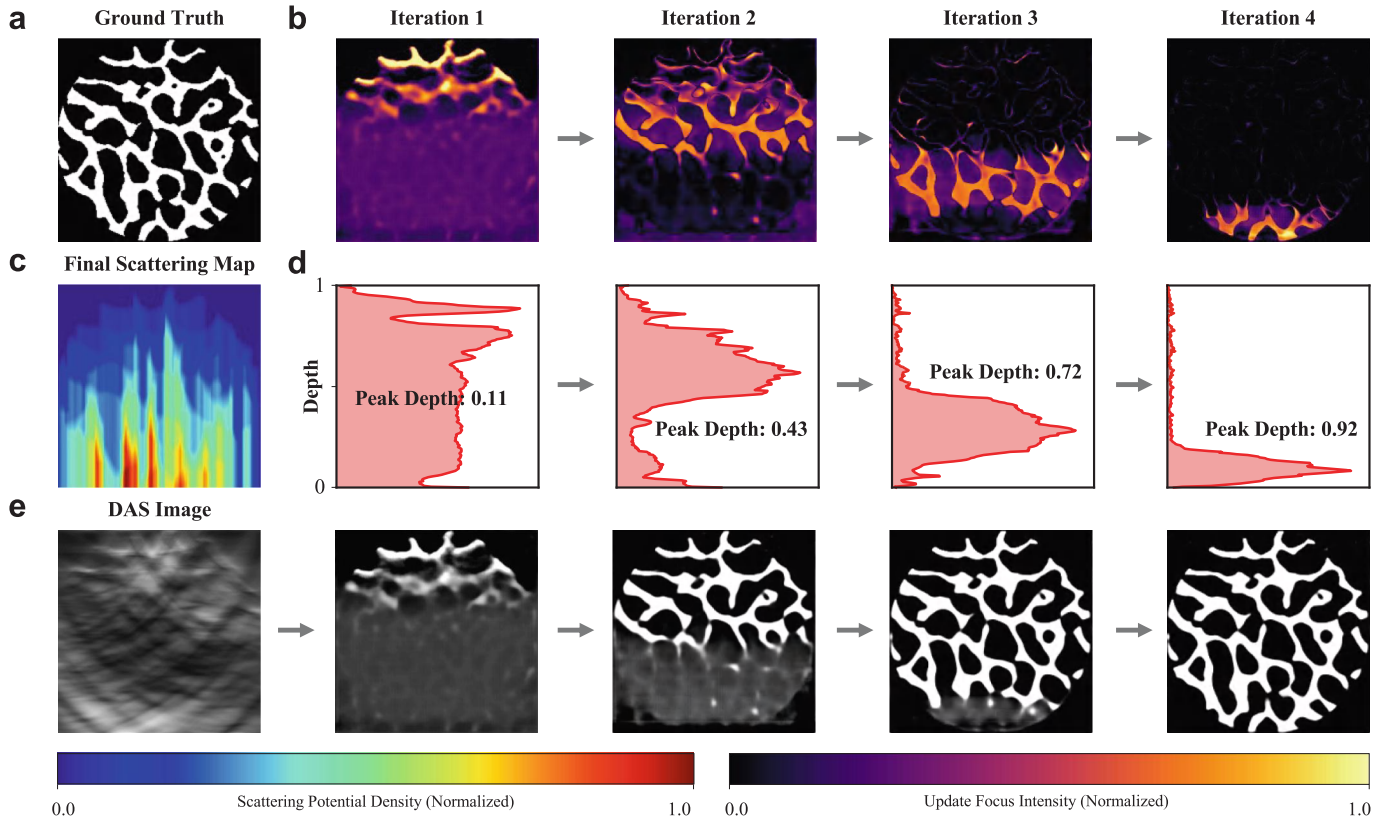


Fig. 5. Iterative reconstruction behavior of LSMS-Net for a representative simulation sample. (a) Ground truth image. (b) Delta update maps at successive iterations, showing that regions with higher update intensity initially appear near the superficial layers and gradually extend toward deeper regions with increasing iteration number. (c) Final estimated scattering map. (d) Depth-wise brightness distributions of the delta update map across iterations, where the peak of the distribution shifts toward greater depths. (e) Comparative visualization of the DAS reconstruction (leftmost) and LSMS-Net intermediate reconstructions from iteration 1 to iteration 4 (left to right), illustrating the progressive extension of reconstructed structures from shallow to deeper regions.

0.91 g/cm^3, longitudinal sound speed ≈ 1450 m/s [44]) to construct a two-phase porous medium, thereby simulating a structure with significant acoustic heterogeneity. PA signals were acquired using a 128-element linear array transducer (center frequency: 3 MHz, −6 dB bandwidth: 60%) and reconstructed by DAS algorithm. High-resolution μ-CT scans of each assembled phantom served as the structural ground truth for validation. The final experimental dataset comprises 1870 independent samples. The full experimental setup is illustrated in Fig. 3b.

Results: Fig. 6(a) shows representative reconstruction results from experiments conducted on 3D-printed phantoms with solid–liquid two-phase porous microstructures. The first image shows the ground truth images. The DAS reconstructions, shown in the second image, serve as

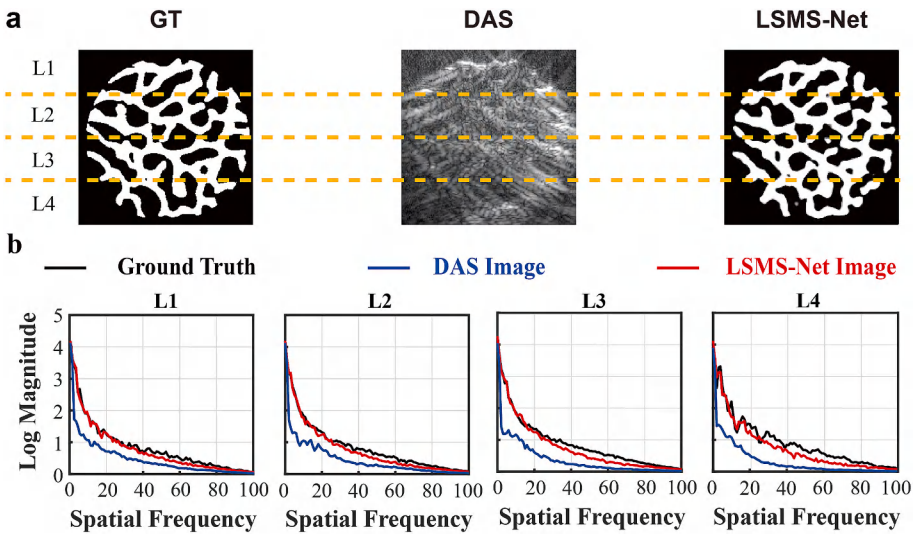


Fig. 6. PAI experiment results from 3D-printed solid–liquid two-phase porous phantoms. (a) From left to right: ground truth (GT), DAS reconstruction (network input), and LSMS-Net reconstruction (network output). DAS reconstructions exhibit severe degradation and loss of fine structural details, particularly at greater depths. LSMS-Net improves structural clarity and continuity across the imaging depth. (b) Depth-resolved spatial frequency profiles extracted from representative axial slices (indicated by dashed lines L1-L4 in (a)) of the representative sample for ground truth, DAS, and LSMS-Net, showing improved preservation of mid- and high-frequency components by LSMS-Net across all depths.

the network input and exhibit pronounced degradation due to strong acoustic scattering, particularly in deeper regions where fine structural details are largely distorted. The third provides the corresponding LSMS-Net reconstructions. Compared with DAS, LSMS-Net recovers clear porous structures across the full imaging depths, including regions where the DAS reconstructions suffer from severe blurring, contrast attenuation, and spatial resolution loss. To quantitatively assess depth-dependent reconstruction performance, spatial frequency profiles extracted along the axial (depth) direction from the last column sample are plotted in Fig. 6(b). As shown, the DAS reconstruction displays significant attenuation of mid- and high- spatial-frequency components with increasing depths, reflecting cumulative scattering-induced resolution degradation. In contrast, LSMS-Net reconstructions preserve high-spatial-frequency content more effectively and exhibit a frequency distribution closer to that of the ground truth.

3.4. Performance comparison

For fair comparison, the ResUNet baseline adopted the same architecture and depth as the Solver module shown in Fig. 2(d), but without the iterative physical synthesis framework. The U-Net baseline followed a conventional encoder–decoder architecture [26] with the same network depth. LSMS-Net and ResUNet were trained for 200 epochs, while U-Net was trained for 500 epochs to ensure convergence. All methods used the same training, validation, and testing datasets and were optimized using Adam with an initial learning rate of 1×10^{-4} and a batch size of 16.

Fig. 7 compares the reconstruction performance of LSMS-Net with

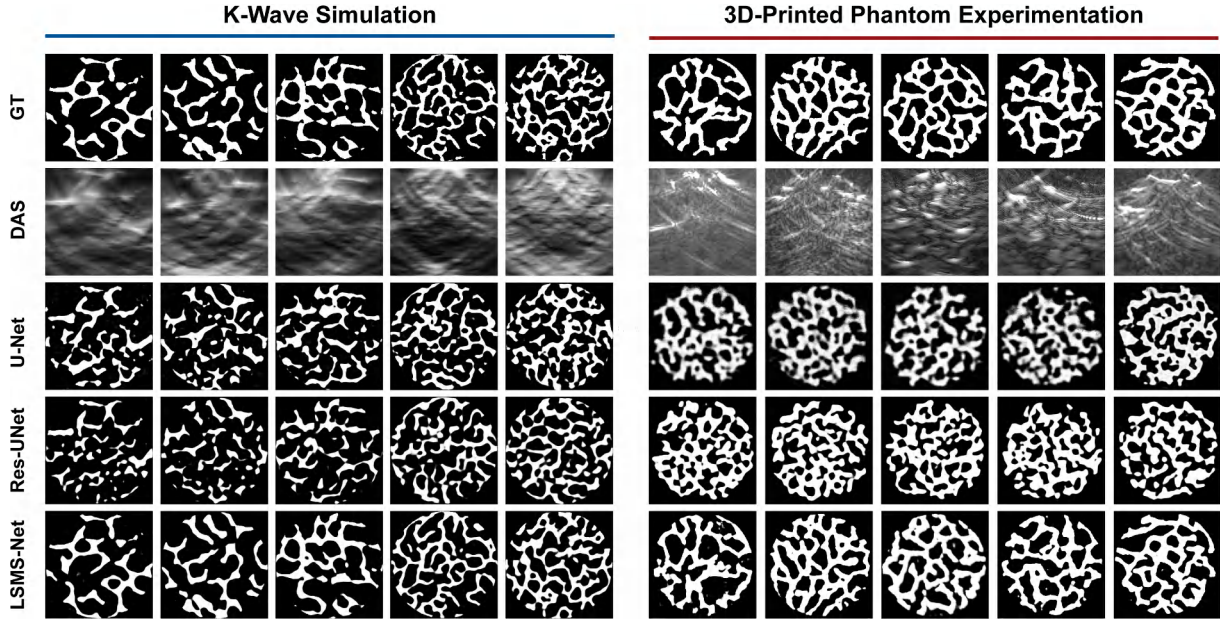


Fig. 7. Comparison of reconstruction results obtained using different methods on k-Wave simulations and 3D-printed phantom experiments. From top to bottom: Ground truth, DAS reconstructions, U-Net reconstructions, ResUNet reconstructions, and LSMS-Net reconstructions.

representative baseline methods including DAS, U-Net, and ResUNet on both k-Wave simulation data and experimental data acquired from 3D-printed phantoms. For each dataset, the first row shows the high-resolution μ-CT-derived ground truth, subsequent rows present reconstructions obtained using DAS (row 2), U-Net (row 3), ResUNet (row 4), and LSMS-Net (row 5). In the k-Wave simulations, the pure physical reconstruct algorithm, DAS, exhibits severe degradation due to acoustic velocity heterogeneity and multiple scattering, resulting in structural blurring, discontinuous pore pathways, and progressive loss of interconnectivity with depth. While U-Net and ResUNet, which both are pure data-driven methods, partially recover superficial structures but show distortions and inconsistencies in deeper regions. In contrast, LSMS-Net consistently restores clear and continuous porous structures that closely resemble the ground truth across different simulation conditions.

Similar trends are observed in the 3D-printed phantom experiments study. DAS struggles to capture meaningful structure due to unmitigated scattering artifacts, while purely data-driven networks tend to yield fragmented or distorted results. LSMS-Net, however, robustly reconstructs the true porous architecture with accurate pore geometry, spatial coherence, and structural integrity across the entire imaging depth, demonstrating physics-aware generalization.

Quantitative comparisons of reconstruction performance are summarized in Table 1. The evaluation utilizes three complementary image fidelity metrics: PSNR, SSIM, and MS-SSIM. Metrics were computed on both k-Wave simulation data and experimentally acquired data from the 3D-printed phantom. Across all datasets and evaluated metrics, LSMS-Net achieves the best overall performance. Consistent improvements are observed for LSMS-Net compared with DAS and purely data-driven networks, including U-Net and ResUNet. These quantitative results are in agreement with the qualitative observations in Fig. 7, further confirming the superior reconstruction fidelity of LSMS-Net under strong scattering conditions.

4. Discussion

In multi-layered or two-phase porous media, PAI faces a fundamental challenge because optical absorbers simultaneously act as acoustic sources and scatterers, which no longer satisfies the single-scattering assumption commonly adopted in conventional reconstruction methods. To address this, the proposed Layer-Stripping Multi-Scattering Network (LSMS-Net) reformulates image reconstruction as a recursive, physics-constrained inverse scattering problem rather than a single-step enhancement.

Numerical simulations using k-Wave in Fig. 4 demonstrate that scattering-induced degradation persists across a wide range of porosities (60–75%). While DAS reconstructions suffer from severe blurring and loss of structure in deeper regions, LSMS-Net recovers more continuous microstructures across all tested conditions. These observations suggest that incorporating physical constraints into the reconstruction process can improve stability under heterogeneous scattering environments, particularly when multiple scattering effects accumulate with depth.

Table 1
Quantitative comparisons of reconstruction performance.

	k-Wave Simulation			3D-Printed Phantom Experiment		
	PSNR	SSIM	MS-SSIM	PSNR	SSIM	MS-SSIM
DAS	7.14 ± 0.42	0.048 ± 0.014	0.133 ± 0.024	6.41 ± 0.35	0.023 ± 0.007	0.127 ± 0.048
U-Net	6.14 ± 0.98	0.380 ± 0.044	0.373 ± 0.055	5.75 ± 0.55	0.182 ± 0.046	0.331 ± 0.076
ResUNet	6.38 ± 0.88	0.416 ± 0.051	0.373 ± 0.053	5.34 ± 0.48	0.345 ± 0.032	0.322 ± 0.067
LSMS-Net	**18.13 ± 0.97**	**0.874 ± 0.021**	**0.974 ± 0.006**	**15.73 ± 3.49**	**0.789 ± 0.121**	**0.922 ± 0.084**

Besides reconstruction quality, the iterative behavior visualized in Fig. 5 provides insight into how LSMS-Net operates. The progressive extension of reconstructed structures from shallow to deeper regions, together with the downward shift of the update energy across iterations, suggests that the network follows a layer-stripping process. By embedding a differentiable, physics-based forward scattering simulator within each iteration, LSMS-Net is able to leverage reconstructed shallow-layer structures to estimate their scattering contributions and iteratively account for them in the measured data. This depth-aware refinement process decouples the source contribution from the scatterer-induced interference, which enables the recovery of deeper-layer structures under cumulative multiple scattering. Such behavior is distinct from conventional data-driven feed-forward networks, which lack explicit mechanisms to enforce depth-dependent physical consistency or causal wave propagation constraint.

Experimental validation using the 3D-printed phantoms in Fig. 6(b) indicate that the proposed approach maintains its reconstruction performance under experimental noise and transducer bandwidth limitations. The accompanying depth-resolved spatial frequency analysis further supports the effectiveness of the spectral consistency constraint, particularly in preserving mid- and high-frequency components in deeper regions where conventional reconstructions exhibit substantial attenuation. These results are consistent with the expectation that enforcing physically plausible spectral behavior can help regularize the reconstruction process in strongly scattering media.

Comparisons with baseline deep learning methods (Fig. 7) highlight the limitations of purely data-driven approaches under strong multiple scattering. Although U-Net and ResUNet partially recover superficial structures, their reconstructions exhibit increasing fragmentation and structural inconsistency in deeper regions, likely due to the highly non-local and depth-dependent nature of the forward propagation process. In contrast, LSMS-Net constrains the solution space through embedded physical modeling, which reduces the tendency to generate structures that are inconsistent with the measured data and underlying wave physics. This distinction underscores the importance of integrating physics-based constraints when addressing inverse problems dominated by multiple scattering.

Although LSMS-Net achieved consistent improvement in both k-Wave simulations and 3D-printed phantom experiments, the current study remains a controlled validation stage, and the present framework was specifically designed for porous bone-like structures. In this model, the PA source distribution was simplified by assuming the μ-CT-derived trabecular bone structures were the primary optical absorbers. This assumption is reasonable for porous bone-like structures where PA signal-generating structures are closely associated with acoustic scatterers. However, optical absorbers and scatterers in many biological tissues may be from different structures. Recent deep learning studies have shown the feasibility of recovering PA sources through strongly scattering media with spatially separated absorbers and scatterers [13,45]. This work addresses the complementary scenario where the scattering structures are the imaging targets. Future integration of these two directions may extend LSMS-Net to more general tissue imaging scenarios. In addition, multiple endogenous absorbers may contribute to PA signal generation under a single wavelength. Nevertheless, multi-spectral PA imaging [46] and deep learning-driven quantitative spectroscopic PA methods [47] provide feasible routes to separate or quantify different absorber contributions in future extensions. Furthermore, the current experiments do not fully include practical system-dependent degradations, such as electronic noise, sparse acquisition and finite transducer bandwidth. Previous studies have shown that deep learning can suppress PA noise, enhance low-fluence images, and compensate for limited-view and bandwidth-related visibility artifacts [48,49]. Moreover, although the phantom experiments used 3D-printed samples, the reconstruction and evaluation were based on two-

dimensional cross-sectional representations, which do not fully capture out-of-plane acoustic propagation in 3D heterogeneous tissues. Therefore, future work will focus on validation using realistic 3D tissue-like, ex vivo, and in vivo datasets for further training, fine-tuning, and evaluation.

Overall, LSMS-Net demonstrates the ability to recover porous bone-like microstructures from strongly scattered PA measurements by incorporating layer-stripping reconstruction and physics-informed constraints. This capability may provide a useful basis for non-invasive and radiation-free microstructural imaging in bone-related applications, such as osteoporosis associated with cancer metastasis and aging-related bone deterioration. Future studies using more realistic tissue models and biological datasets will further facilitate the evaluation of its performance in practical imaging scenarios.

5. Conclusion

In this work, we developed the Layer-Stripping Multi-Scattering Network (LSMS-Net), a physics-constrained deep learning framework for PAI in heterogeneous multi-layer and two-phase porous media. Unlike conventional single-step beamforming or purely data-driven methods based on weak, localized, or single-scattering assumptions, LSMS-Net treats image reconstruction as a recursive inverse scattering process guided by wave physics. By explicitly accounting for the dual role of absorbers as both acoustic sources and scatterers during reconstruction, our method effectively corrects scattering-induced degradation that is difficult to address with conventional reconstruction models.

Central to LSMS-Net is an analysis-by-synthesis strategy that progressively accounts for scattering effects during reconstruction. Through the integration of iterative forward scattering modeling and spectral consistency constraints, the proposed approach enables the recovery of structurally coherent and physically meaningful features, particularly in deeper regions where conventional reconstruction methods experience severe information loss under strong multiple scattering.

Extensive validation on k-Wave simulations and complex 3D-printed porous phantoms demonstrates that LSMS-Net consistently outperforms traditional reconstruction algorithms and standard deep learning models under strong scattering conditions. These results indicate that embedding physical constraints into the reconstruction process is essential for achieving robust and reliable PAI in highly heterogeneous distributed sources environments.

LSMS-Net provides a physics-constrained reconstruction framework for scattering-dominated PAI in porous media. Future work will extend the framework to full 3D volumetric reconstruction and validate its performance in preclinical in vivo models to further evaluate its robustness and translational potential.

Author contributions

Wenyi Xu contributed to the design, planning, and the execution of the network training, performed experiment, data processing and prepared the manuscript. Weiya Xie contributed to the simulation design and revised the manuscript. Renzhe Bi and Malini Olivo contributed to the phantom experiments and revised the manuscript. Lifang Jin and Shengsong Huang provided the medical guidance and revised the manuscript. Ya Gao contributed to the network training and revised the manuscript. Qian Cheng supervised the project and revised the manuscript.

CRediT authorship contribution statement

Wenyi Xu: Writing – review & editing, Writing – original draft, Visualization, Validation, Methodology, Investigation, Formal analysis, Data curation, Conceptualization. **Renzhe Bi:** Writing – review & editing, Supervision, Resources, Methodology. **Weiya Xie:** Writing – review & editing, Investigation, Formal analysis, Data curation. **Lifang Jin:** Writing – review & editing, Conceptualization. **Malini Olivo:** Writing – review & editing, Supervision, Resources. **Shengsong Huang:** Writing – review & editing, Conceptualization. **Ya Gao:** Writing – review & editing, Visualization, Validation, Data curation. **Qian Cheng:** Writing – review & editing, Supervision, Resources, Project administration, Funding acquisition.

Declaration of Generative AI and AI-assisted technologies in the writing process

During the preparation of this work the author used ChatGPT in order to polish the language. After using this tool, the author reviewed and edited the content as needed and takes full responsibility for the content of the publication.

Declaration of competing interest

The authors declare that they have no known competing financial interests or personal relationships that could have appeared to influence the work reported in this paper.

Acknowledgments

This study was supported by the National Natural Science Foundation of China [grant numbers 12034015], and the Natural Science Foundation of Shandong Province (Grant No. ZR2024QA049).

Appendix A. Supplementary data

Supplementary data to this article can be found online at https://doi.org/10.1016/j.ultras.2026.108241.

Data availability

Data underlying the results presented in this paper are not publicly available at this time but may be obtained from the author upon reasonable request.

References

[1] C. Kim, C. Favazza, L.V. Wang, In vivo photoacoustic tomography of chemicals: high-resolution functional and molecular optical imaging at new depths, Chem. Rev. 110 (2010) 2756–2782, https://doi.org/10.1021/cr900266s.
[2] Zhang R, A'dawiah R, Choo TWJ, et al. Navigating challenges and solutions in quantitative photoacoustic imaging. Appl Phys Rev 2024;11:031308. https://doi.org/10.1063/5.0202401.
[3] S. Manohar, S.E. Vaartjes, J.C.G. van Hespen, et al., Initial results of in vivo non-invasive cancer imaging in the human breast using near-infrared photoacoustics, Opt. Express 15 (2007) 12277, https://doi.org/10.1364/OE.15.012277.
[4] L.V. Wang, J. Yao, A practical guide to photoacoustic tomography in the life sciences, Nat. Methods 13 (2016) 627–638, https://doi.org/10.1038/nmeth.3925.
[5] J. Shubert, M.A.L. Bell, Photoacoustic imaging of a human vertebra: implications for guiding spinal fusion surgeries, Phys. Med. Biol. 63 (2018) 144001, https://doi.org/10.1088/1361-6560/aacdd3.
[6] T. Feng, Y. Zhu, Y. Xie, et al., Feasibility study for bone health assessment based on photoacoustic imaging method, Chin. Opt. Lett. 18 (2020) 121704, https://doi.org/10.3788/COL202018.121704.
[7] C. Chai, X. Yang, X. Gao, et al., Enhancing photoacoustic imaging for lung diagnostics and BCI communication: simulation of cavity structures artifact generation and evaluation of noise reduction techniques, Front. Bioeng. Biotechnol. 12 (2024) 1452865, https://doi.org/10.3389/fbioe.2024.1452865.
[8] S. Wang, T. Tran, L. Xiang, et al., in: Non-Destructive Evaluation of Composite and Metallic Structures Using Photo-Acoustic Method, American Institute of Aeronautics and Astronautics, San Diego, California, 2019, https://doi.org/10.2514/6.2019-2042.
[9] N. Aminoroaya, H. Ehtesabi, R. Monfared-Hajishirkiaee, et al., Investigating the absorbent properties of carboxymethyl cellulose-chitosan-carbon dots nanocomposite sponge using photoacoustic microscopy, Int. J. Biol. Macromol. 308 (2025) 142517, https://doi.org/10.1016/j.ijbiomac.2025.142517.
[10] P.C. Tay, S.T. Acton, J.A. Hossack, A wavelet thresholding method to reduce ultrasound artifacts, Comput. Med. Imaging Graph. 35 (2011) 42–50, https://doi.org/10.1016/j.compmedimag.2010.09.003.
[11] S. Govinahallisathyanarayana, B. Ning, R. Cao, et al., Dictionary learning-based reverberation removal enables depth-resolved photoacoustic microscopy of

cortical microvasculature in the mouse brain, Sci. Rep. 8 (2018) 985, https://doi.org/10.1038/s41598-017-18860-3.
[12] G.S. He, H.-Y. Qin, Q. Zheng, Rayleigh, Mie, and Tyndall scatterings of polystyrene microspheres in water: wavelength, size, and angle dependences, J. Appl. Phys. 105 (2009) 023110, https://doi.org/10.1063/1.3068473.
[13] Y. Gao, W. Xu, Y. Chen, et al., Deep learning-based photoacoustic imaging of vascular network through thick porous media, IEEE Trans. Med. Imaging 41 (2022) 2191–2204, https://doi.org/10.1109/TMI.2022.3158474.
[14] R. Ali, T. Brevett, L. Zhuang, et al., Aberration correction in diagnostic ultrasound: a review of the prior field and current directions, Z Für. Med. Phys. 33 (2023) 267–291, https://doi.org/10.1016/j.zemedi.2023.01.003.
[15] D.E. Soulioti, R.M. Jones, G.F. Pinton, Quantification of the relative contribution of phase aberration and reverberation in transcranial ultrasound imaging: an experimentally calibrated fullwave study in 2D and 3D, Phys. Med. Biol. 70 (2025) 165010, https://doi.org/10.1088/1361-6560/adf2f3.
[16] W. Xu, W. Xie, D. Yu, et al., Theoretical and experimental study of attenuation in cancellous bone, J. Biomed. Opt. 29 (2024) S11526, https://doi.org/10.1117/1.JBO.29.S1.S11526.
[17] M. Xu, L.V. Wang, Universal back-projection algorithm for photoacoustic computed tomography, Phys. Rev. E 71 (2005) 016706, https://doi.org/10.1103/PhysRevE.71.016706.
[18] W. Choi, D. Oh, C. Kim, Practical photoacoustic tomography: realistic limitations and technical solutions, J. Appl. Phys. 127 (2020) 230903, https://doi.org/10.1063/5.0008401.
[19] X.L. Deán-Ben, V. Ntziachristos, D. Razansky, Effects of small variations of speed of sound in optoacoustic tomographic imaging: small speed of sound variations in optoacoustic tomography, Med. Phys. 41 (2014) 073301, https://doi.org/10.1118/1.4875691.
[20] Y. Hristova, P. Kuchment, L. Nguyen, Reconstruction and time reversal in thermoacoustic tomography in acoustically homogeneous and inhomogeneous media, Inverse Probl. 24 (2008) 055006, https://doi.org/10.1088/0266-5611/24/5/055006.
[21] C. Huang, K. Wang, L. Nie, et al., Full-wave iterative image reconstruction in photoacoustic tomography with acoustically inhomogeneous media, IEEE Trans. Med. Imaging 32 (2013) 1097–1110, https://doi.org/10.1109/TMI.2013.2254496.
[22] J. Poudel, S. Na, L.V. Wang, et al., Iterative image reconstruction in transcranial photoacoustic tomography based on the elastic wave equation, Phys. Med. Biol. 65 (2020) 055009, https://doi.org/10.1088/1361-6560/ab6b46.
[23] X.L. Dean-Ben, A. Buehler, V. Ntziachristos, et al., Accurate model-based reconstruction algorithm for three-dimensional optoacoustic tomography, IEEE Trans. Med. Imaging 31 (2012) 1922–1928, https://doi.org/10.1109/TMI.2012.2208471.
[24] L. Ding, D. Razansky, X.L. Dean-Ben, Model-based reconstruction of large three-dimensional optoacoustic datasets, IEEE Trans. Med. Imaging 39 (2020) 2931–2940, https://doi.org/10.1109/TMI.2020.2981835.
[25] H. Park, J. Yao, Y. Jing, A frequency-domain model-based reconstruction method for transcranial photoacoustic imaging: a 2D numerical investigation, Photoacoustics 33 (2023) 100561, https://doi.org/10.1016/j.pacs.2023.100561.
[26] Ronneberger O, Fischer P, Brox T. U-Net: Convolutional Networks for Biomedical Image Segmentation. In: Navab N, Hornegger J, Wells WM, et al., editors. Med. Image Comput. Comput.-Assist. Interv. – MICCAI 2015, vol. 9351, Cham: Springer International Publishing; 2015, p. 234–41. https://doi.org/10.1007/978-3-319-24574-4_28.
[27] P. Chen, C. Liu, T. Feng, et al., Improved photoacoustic imaging of numerical bone model based on attention block U-net deep learning network, Appl. Sci. 10 (2020) 8089, https://doi.org/10.3390/app10228089.
[28] J. Kim, G. Kim, L. Li, et al., Deep learning acceleration of multiscale superresolution localization photoacoustic imaging, Light Sci. Appl. 11 (2022) 131, https://doi.org/10.1038/s41377-022-00820-w.
[29] A. Hauptmann, F. Lucka, M. Betcke, et al., Model-based learning for accelerated, limited-view 3-D photoacoustic tomography, IEEE Trans. Med. Imaging 37 (2018) 1382–1393, https://doi.org/10.1109/TMI.2018.2820382.
[30] K. Wang, M.A. Anastasio, Photoacoustic and thermoacoustic tomography: image formation principles, Springer, Handb. Math. Methods Imaging, 2011, pp. 781–815.
[31] B.T. Cox, S. Kara, S.R. Arridge, et al., k -space propagation models for acoustically heterogeneous media: application to biomedical photoacoustics, J. Acoust. Soc. Am. 121 (2007) 3453–3464, https://doi.org/10.1121/1.2717409.
[32] Yu F, Koltun V. Multi-Scale Context Aggregation by Dilated Convolutions, 2016. https://doi.org/10.48550/arXiv.1511.07122.
[33] A. Ishimaru, Wave propagation and scattering in random media, Academic Press, New York, 1978.
[34] K.C. Diagnostic, U. Imaging, Inside out, Ultrasound Med. Biol. 41 (2015) 622, https://doi.org/10.1016/j.ultrasmedbio.2014.09.026.
[35] B.E. Treeby, B.T. Cox, k-Wave: MATLAB toolbox for the simulation and reconstruction of photoacoustic wave fields, J. Biomed. Opt. 15 (2010) 021314, https://doi.org/10.1117/1.3360308.
[36] T. Feng, Y. Zhu, R. Morris, et al., The feasibility study of the transmission mode photoacoustic measurement of human calcaneus bone in vivo, Photoacoustics 23 (2021) 100273, https://doi.org/10.1016/j.pacs.2021.100273.
[37] W. Xie, T. Feng, M. Zhang, et al., Wavelet transform-based photoacoustic time-frequency spectral analysis for bone assessment, Photoacoustics 22 (2021) 100259, https://doi.org/10.1016/j.pacs.2021.100259.
[38] G. Haïat, A. Lhémery, F. Renaud, et al., Velocity dispersion in trabecular bone: influence of multiple scattering and of absorption, J. Acoust. Soc. Am. 124 (2008) 4047–4058, https://doi.org/10.1121/1.3003077.
[39] D. Hans, C. Wu, C.F. Njeh, et al., Ultrasound velocity of trabecular cubes reflects mainly bone density and elasticity, Calcif. Tissue Int. 64 (1999) 18–23, https://doi.org/10.1007/s002239900572.
[40] L. Cardoso, F. Teboul, L. Sedel, et al., In vitro acoustic waves propagation in human and bovine cancellous bone, J. Bone Miner. Res. 18 (2003) 1803–1812, https://doi.org/10.1359/jbmr.2003.18.10.1803.
[41] D. Porrelli, M. Abrami, P. Pelizzo, et al., Trabecular bone porosity and pore size distribution in osteoporotic patients – a low field nuclear magnetic resonance and microcomputed tomography investigation, J. Mech. Behav. Biomed. Mater. 125 (2022) 104933, https://doi.org/10.1016/j.jmbbm.2021.104933.
[42] D. Ma, R. Gao, M. Li, et al., Mechanical and medical imaging properties of 3D-printed materials as tissue equivalent materials, J. Appl. Clin. Med. Phys. 23 (2022) e13495, https://doi.org/10.1002/acm2.13495.
[43] H. Ramezani Dana, F. Ebrahimi, Synthesis, properties, and applications of polylactic acid-based polymers, Polym. Eng. Sci. 63 (2023) 22–43, https://doi.org/10.1002/pen.26193.
[44] J. Yan, W.M.D. Wright, J.A. O'Mahony, et al., A sound approach: exploring a rapid and non-destructive ultrasonic pulse echo system for vegetable oils characterization, Food Res. Int. 125 (2019) 108552, https://doi.org/10.1016/j.foodres.2019.108552.
[45] P. Wan, F. Zhang, Y. Shen, et al., HDN: hybrid deep-learning and non-line-of-sight reconstruction framework for transcranial photoacoustic imaging of human brain, IEEE Trans. Comput. Imaging 11 (2025) 1142–1149, https://doi.org/10.1109/TCI.2025.3594073.
[46] L. Ding, X.L. Deán-Ben, N.C. Burton, et al., Constrained inversion and spectral unmixing in multispectral optoacoustic tomography, IEEE Trans. Med. Imaging 36 (2017) 1676–1685, https://doi.org/10.1109/TMI.2017.2686006.
[47] R. Shang, S. Jandhyala, Y. Wu, et al., Deep learning-driven quantitative spectroscopic photoacoustic imaging for segmentation and oxygen saturation estimation, Ultrasonics 165 (2026) 108092, https://doi.org/10.1016/j.ultras.2026.108092.
[48] C. Tian, K. Shen, W. Dong, et al., Image reconstruction from photoacoustic projections, Photonics Insights 3 (2024) R06, https://doi.org/10.3788/PI.2024.R06.
[49] Y. Yu, T. Feng, H. Qiu, et al., Simultaneous photoacoustic and ultrasound imaging: a review, Ultrasonics 139 (2024) 107277, https://doi.org/10.1016/j.ultras.2024.107277.